11-1-2010

Rare Earth and High Field Strength Element Partitioning Between Iron-Rich Clinopyroxenes and Felsic Liquids

Paul H. Olin
Boise State University

John A. Wolff
Washington State University

Rare Earth and High Field Strength Element Partitioning Between Iron-Rich Clinopyroxenes and Felsic Liquids

Paul H. Olin
Boise State University

J.A. Wolff
Washington State University

Abstract

Rare earth elements are commonly assumed to substitute only for Ca in clinopyroxene because of the similarity of ionic radii for REE^{3+} and Ca^{2+} in 8-fold coordination. The assumption is valid for Mg-rich clinopyroxenes for which observed mineral/melt partition coefficients are readily predicted by the lattice strain model for substitution onto a single site (e.g. Wood and Blundy, 1997). We show that natural Fe-rich pyroxenes in both silica-undersaturated and –oversaturated magmatic systems deviate from this behavior. Salites (Mg# 48 to 59) in phonolites from Tenerife, ferrohedenbergites (Mg# 14.2 to 16.2) from the rhyolitic Bandelier Tuff, and ferroaugites (Mg# 9.6 to 32) from the rhyolitic Rattlesnake Tuff have higher heavy REE contents than predicted by single-site substitution. The ionic radius of Fe^{2+} in 6-fold coordination is substantially greater than that of Mg^{2+}, hence we propose that, in Fe-rich clinopyroxenes, heavy REE are significantly partitioned between 8-fold Ca sites and 6-fold Fe-Mg sites such that Yb and Lu exist dominantly in 6-fold coordination. We also outline a REE-based method of identifying pyroxene-melt pairs in systems with multiple liquid and crystal populations, based upon the assumption that LREE and MREE reside exclusively in 8-fold coordination in pyroxene.

Contrary to expectations, interpolation of mineral/melt partition coefficient data for heavy REE does not predict the behavior of Y. We speculate that mass fractionation effects play a role in mineral/melt lithophile trace element partitioning that is detectable among pairs of isovalent elements with near-identical radii, such as Y-Ho, Zr-Hf, and Nb-Ta.

Introduction

Clinopyroxene is one of the most abundant minerals in igneous rocks and plays a major role in the generation and subsequent differentiation of magma. Trace element partitioning between clinopyroxene and silicate liquid has therefore been the subject of intense study, especially since the successful application of lattice strain theory (Brice, 1975; Blundy and Wood, 1994) to crystal-melt element partitioning in igneous systems (Gaetani and Grove, 1995; Wood and Blundy, 1997, 2001, 2002; Blundy et al., 1998; Lundstrom et al., 1998; Hill et al., 2000; Pertermann and Hirschmann, 2002). Most of these studies focus on Mg-rich clinopyroxene and its role in influencing lithophile trace element abundances in basaltic magma. Consequently, the partitioning of rare earth elements into Mg-rich clinopyroxene is well characterized: light REE are incompatible, but compatibility increases with atomic number, typically flattening out between Ho and Lu (Fig. 1). In contrast, Fe-rich clinopyroxenes from many strongly differentiated systems show somewhat different behavior; the value of the partition coefficient D [=(concentration in solid phase)/(concentration in liquid), C_s/C_l] rises with atomic number from the light to the middle REE, flattens out or declines slightly between Gd and Ho-Er, and distinctly rises to higher values at Yb and Lu (Fig. 1). Here, we describe enhanced heavy REE contents in natural Fe-rich clinopyroxene from phonolites and rhyolites. In Mg-rich clinopyroxene, REE are assumed to reside exclusively in 8-fold coordination on the M2 structural site. We show that the distinctive partitioning behavior of REE into Fe-rich pyroxenes is most simply explained by partial heavy REE occupancy of 6-

fold coordinated sites with radii near those of Fe^{2+} and Mn^{2+}; these may be located on either the M2 or M1 site (Cameron and Papike, 1980). We then describe a method for identifying equilibrium pyroxene-glass pairs on the basis of the complementary assumption that light and middle REE reside exclusively in 8-fold coordination. We also demonstrate significant Y/Ho, Zr/Hf and Nb/Ta fractionation between clinopyroxene and melt, and speculate that factors other than ionic radius and charge have a detectable effect on mineral-melt partitioning behavior of lithophile element cations.

Samples

Pyroxenes and glasses in this study come from three volcanic systems: Na-salites from the phonolitic Fasnia Member of the Diego Hernández Formation, Tenerife, Spain; ferrohedenbergites from the high-silica rhyolitic Bandelier Tuff, New Mexico, USA; and ferroaugites to ferrohedenbergites from the rhyolitic Rattlesnake Tuff, Oregon, USA.

Information about each system is summarized in Table 1. The three magmas are all close to minimum melt compositions with (Na + K)/Al ≈ 1 and near-identical degrees of melt polymerization as indicated by the parameter NBO/T, but vary strongly in alkali content and silica saturation.

Fasnia Member, Tenerife

The 309 ± 6 ka Fasnia Member (FM) is one of the major units of the phonolitic, caldera-related Diego Hernández Formation of the Las Cañadas Upper Group on Tenerife (Martí et al., 1994; Edgar et al., 2007). Las Cañadas phonolites have whole-rock compositions that lie close to the 1 kbar water-saturated phonolitic minimum in the *ne-ks-Q* system (Hamilton & MacKenzie, 1965), oxygen fugacities that lie close to the NNO buffer (Wolff & Storey, 1983) and temperatures typically in the range 790 – 850°C (Wolff & Storey, 1983; Bryan, 2006; Andújar et al., 2008). In addition to the phenocryst phases listed in Table 1, the FM contains trace amounts of apatite and pyrrhotite as inclusions in other minerals. The FM is the product the explosive eruption of ~13 km^3 of phonolite magma with a large range in trace element abundances (Edgar et al., 2007), due to mixing of at least two distinct end member phonolites and a small volume of mafic magma that resulted in a dominant volume of hybrid phonolite (Olin, 2007). Despite variable trace element contents (Table 2), fresh FM glasses considered here exhibit very little variation in major elements, with approximately 15 wt.% total alkalies and (Na + K)/Al ≈ 1.

Sodian salites analyzed in this study have near-constant major element compositions (Fig. 2) and trace element contents that are consistent with having crystallized from the hybrid FM magma (Olin, 2007). Individual pyroxene grains are euhedral and do not display detectable zoning in either major or trace elements.

Bandelier Tuff

The ~450 km^3 Otowi Member of the Bandelier Tuff (BT) erupted from the Valles caldera, New Mexico, at 1.61 Ma. The BT is a high-silica rhyolite with a composition that closely corresponds to the water-saturated granite minimum between 1 and 2 kbar (Tuttle & Bowen, 1958). The phenocryst assemblage contains quartz, magnetite and fayalite and fO_2 is therefore presumed to lie close to the QMF buffer. Trace amounts of zircon and allanite occur in addition to the phenocrysts listed in Table 1, and chevkinite and britholite are present as inclusions in clinopyroxene, fayalite, and magnetite (Min et al., 2006). The tuff displays strong vertical zonation in incompatible trace elements (Spell et al., 1990; Wolff et al., 1999); euhedral ferrohedenbergites and glasses analyzed in this study come from the most differentiated, chemically homogeneous, first-erupted portion of the magma body.

Rattlesnake Tuff

The 7.05 Ma Rattlesnake Tuff (RT) represents the explosive eruption of ~280 km^3 of multi-component rhyolitic magma (Streck & Grunder, 1997, 2007). The RT contains five distinct high silica rhyolite compositions, A, B, C, D, and E (Streck & Grunder 1997), related primarily by fractional crystallization where type A rhyolite is the most differentiated and type E is the least differentiated. Glasses and

pyroxenes from RT rhyolites type C, D, and E were analyzed in this study, and due to their similarities in trace element contents, respectively (Streck & Grunder, 1997), are treated as one population. In addition to the phases listed in Table 1, trace amounts of biotite occur in rhyolite types C - E, plus the accessory minerals zircon, chevkinite, apatite and pyrrhotite. The RT pyroxenes span a major-element compositional range from Mg# = 9.6 associated with type E rhyolite with ~74 wt% SiO_2 to pyroxenes with values as high as Mg# = 31.7 in type C rhyolite with ~77 wt% SiO_2.

Analytical Methods

All data were generated in the Washington State University GeoAnalytical Laboratory using laser ablation and solution ICP-MS analysis of trace element concentrations and electron microprobe for major element analysis, except for BT hedenbergite major element microprobe data from Kuentz (1986). Trace element concentrations in FM, BT and RT pyroxenes and FM and BT glasses were measured by ablating shallow (<5 μm deep) troughs with a New Wave 213 nm laser coupled to an Element2 high-resolution mass spectrometer. For pyroxenes, ablation troughs were 12 to 20 μm wide by 0.5 to 1 mm long. Grains were analyzed *in situ* where encountered in polished sections (for FM and BT samples) or as mineral separates mounted in epoxy (for FM, BT and RT samples). Trace element concentrations in pumiceous glasses from the FM and BT were determined using LA-ICP-MS *in situ* on polished sections. Laser tracks were positioned to follow along bubble walls in pumice resulting in 5 to 8 μm-wide troughs with irregular geometries and lengths of 200 – 500 μm. For both pyroxenes and glasses, acquired counts per second data were reduced offline and internally normalized to the electron microprobe determined SiO_2 contents and laser determined ^{29}Si counts per second. Two-point calibrations were constructed using BCR-2g and either NIST 610 or NIST 612 as standards.

Glass shard separates from the RT were too small for mounting and polishing and their trace element contents were therefore determined using a small-scale dissolution technique on small aliquots (3 to 11 mg) repeated three times for each sample and averaged. Glass separates were dissolved in a two-step digestion process. First, 0.05 ml pure H_2O, 0.1 ml 37% HCl, 0.1 ml 70% HNO_3, 0.25 ml 50% HF, and 0.1 ml 71% $HClO_4$ were added to each sample vial. Vials were capped overnight and held on a hotplate at 130°C, then uncapped and allowed to evaporate to dryness. Next, 0.05 ml pure H_2O and 0.1 ml 70% $HClO_4$ were added, and evaporated to dryness again. The final solutions were gravimetrically diluted to 30 mg in 2% HNO_3 with 4 drops 30% H_2O_2 and 1 drop 50% HF. Solutions were analyzed on an Element2 mass spectrometer coupled to a Cetac Aridus desolvating nebulizer to increase sensitivity and to reduce oxides. International standards BCR-2, BHVO-1, and in-house standard GMP were used for calibration. A comparison of BCR-2g and an in-house pyroxene standard (TFPX4) analyzed by both laser ablation and solution methods is shown in Fig. 3; there is no significant difference in REE contents analyzed by the two methods.

Gadolinium is not used in this study; there are unresolved issues with the ^{157}Gd isotope in many of the laser ablation analyses of both pyroxenes and glasses. Scandium contents in BT glasses are below the detection limits of the laser ablation procedure, while doubly charged zirconium ($^{90}Zr^{2+}$) in the very Zr-rich FM phonolite glasses interferes with ^{45}Sc; consequently, D_{Sc} is only reported for the RT system.

Major elements in FM and RT pyroxenes were measured using a Cameca electron microprobe in the Washington State University GeoAnalytical Laboratory. The instrument was operated at 15kv, using a spot diameter of ~4 microns and a beam current of 12nA.

Pyroxene chemistry

The Fasnia pyroxenes are sodic salites ($Wo_{49}En_{31}Fs_{20}$ to $Wo_{45}En_{28}Fs_{27}$), the BT pyroxenes are ferrohedenbergites to ferroaugites ($Wo_{44}En_{10}Fs_{46}$ to $Wo_{40}En_{10}Fs_{50}$), and RT pyroxenes are ferroaugites to ferrohedenbergites ($Wo_{43}En_{20}Fs_{37}$ to $Wo_{41}En_{6}Fs_{53}$) in the pyroxene quadrilateral of Poldervaart and Hess (1951); see Fig. 2. The RT and BT pyroxenes have similar major and trace element contents, but are significantly different from the Na-salites (Table 2 and Figs. 4), which have higher Na, Mg, Al, and Ti contents, and lower Fe, Mn and Si contents.

Compositional differences between hedenbergites and salites result in contrasting major element cation site assignments. Silicon occupies the T-site and Al makes up any Si shortfall in tetrahedral coordination. Si+Al is approximately equal to 2 pfu for all pyroxenes. M1 hosts all Ti^{4+} and also hosts Fe, Mn, and Mg, but significant Ca+Na shortfalls (<1 pfu) in the hedenbergites require that at least some Fe and Mn, and probably Mg, occupy M2. In the Na-salites this substitution is minor.

For the sake of simplicity and consistency, we calculate Fe^{3+} contents for all the pyroxenes using the stoichiometric assumption of Droop (1987). Approximately 50% of total Fe in the FM pyroxenes, 10% of total Fe in the RT pyroxenes, and <10% of total Fe in the BT pyroxenes is found to be Fe^{3+}. We assume no preferential ordering of Mn, Fe, and Mg into M2 and M1 structural sites in the pyroxenes, rather we calculate sizes for the 6-fold coordinated site from the weighted average of Mn, Fe^{2+}, Fe^{3+}, and Mg contents. All Fe^{3+} is considered to be in 6-fold coordination.

Trace element partitioning between pyroxenes and glasses

Mineral chemistry effects

The lattice structure of clinopyroxene changes in response to changing Fe/Mg and Na/Ca due to the size differences between Na and Ca, and Fe and Mg (Cameron and Papike, 1980). Since Mn is slightly larger than Fe^{2+} (Shannon, 1976), incorporation of Mn must also result in structural changes. These structural changes should have consequences for trace element partitioning behavior, which should therefore differ between Fe-rich and the more common Mg-rich pyroxenes.

Pyroxene has the general formula [M2][M1][T_2O_6]. The tetrahedral site (T) is filled with Si and lesser amounts of ^{IV}Al. The M2 polyhedron is larger and always more distorted than M1 (Cameron and Papike, 1980) and will accommodate VI-, VII- and VIII-coordinated univalent, divalent and trivalent cations with ionic radii from ~0.72 Å (^{VI}Mg) to ~1.16 Å (^{VIII}Na). Sevenfold coordination has only been described for some pigeonites (Cameron and Papike, 1980) and is not considered further here. A preference for either M1 or M2 is influenced by anion configuration around each site, and by the ionic radius and electronegativity of the cations (Cameron and Papike, 1980). M1 is the smaller of the two cation sites and accommodates divalent, trivalent, tetravalent, and pentavalent cations in 6-fold coordination, with ionic radii between ~0.53 Å ($^{VI}Al^{3+}$) and ~0.83 Å ($^{VI}Mn^{2+}$). Larger cations such as ^{VIII}Na (1.18 Å) and ^{VIII}Ca (1.12 Å) will prefer M2 to M1 (Robinson, 1980).

REE partitioning model

In the lattice strain model (LSM) of Brice (1975) and Blundy and Wood (1994), the partition coefficient D_i at equilibrium of a cation with radius r_i entering a particular crystal lattice site M is given by

$$D_i = D_0 * \exp\{-4\pi E_M N_A [r_0(r_i - r_0)^2/2 + (r_i - r_0)^3/3]/RT\} \quad (1)$$

where D_0 is the partition coefficient of an isovalent ion of radius r_0 which enters the site without strain, E_M is the Young's modulus of site M, N_A is Avogadro's Number, R is the universal gas constant, and T is temperature in Kelvin. The relationship is most often plotted on an Onuma diagram as the logarithm of the partition coefficient versus ionic radius, producing a parabolic distribution (Fig. 5a). The partition coefficient D_0 for a cation with optimal radius r_0 fixes the apex of the parabola, and its curvature is controlled by the Young's modulus (E_M) for the site. Larger E_M values 'tighten' the parabola, reflecting greater stiffness of the site and therefore a relatively narrower range of radii for cations that significantly substitute into the site. For the application of the model below, it is not necessary to know r_0 and D_0 *a priori* as long as there are enough elements to plot to define the shape of the parabola.

Numerous studies have successfully applied the LSM to mineral-melt partitioning, especially for Ca-Mg pyroxenes (Wood and Blundy, 1997; Vannucci et al., 1998; Hill et al., 2000; Wood and Trigila, 2001; Tiepolo et al., 2002). These studies report smooth parabolic distributions of log D_i vs. r_i for REE in pyroxenes that can be modeled by assuming that all REE^{3+} are substituting for eight-fold coordinated Ca^{2+}. However, iron rich pyroxenes found in evolved felsic liquids (e.g. Larsen, 1979; Wörner et al., 1983;

Mahood and Stimac, 1990; Fedele et al., 2009) show REE patterns with elevated partition coefficients from Er to Lu, rather than a simple parabolic form (Figs. 1, 6). Because heavy REE have ionic radii more similar to Fe and Mn in 6-fold coordination than Ca in eight-fold coordination (Table 3), we propose that elevated D_{HREE} in Fe-rich pyroxenes reflects enhanced compatibility relative to lighter REE caused by heavy REE occurring in both eight-fold coordination (substituting for Na or Ca in M2) and 6-fold coordination (substituting for Fe and Mn in M1 or M2). If this is the case, then each coordination state ($^{VI}REE^{3+}$ and $^{VIII}REE^{3+}$) is governed by its own LSM equation, and mineral/melt D values are the sum of the two parabolic functions (Figs. 5 & 7).

Identification of pyroxene-glass pairs

Before these relationships can be explored, it is necessary to establish that the pyroxene grains and glasses used to obtain D values represent equilibrium pairs. One possible problem is late crystallization of accessory phases that concentrate REE and would therefore deplete the melt in REE after pyroxene growth. While we cannot completely rule out this effect, we note that it would tend to deplete middle REE in FM glasses and light REE in the rhyolitic glasses, thus enhancing the apparent D values for these elements with respect to heavy REE, the opposite of what we in fact observe. In fact, the FM pyroxenes have a deeper middle REE trough than do the glasses (Fig. 3).

In all three examples, pyroxene grains are euhedral and appear to be in textural equilibrium with the enclosing glass. However, in the case of the compositionally variable Fasnia phonolite, magmatic processes have scrambled crystals and glasses (Olin, 2007), precluding confident identification of mineral-glass pairs based on physical proximity or grain shape. The method outlined below is independent of major element mineral compositions, assumes that the LSM is a good first-order predictor of trace element partition coefficients, and does not rely on textural relationships. A crucial assumption is that the light and middle REE (La – Dy) are not partitioned between 6-fold and 8-fold sites, but reside exclusively on the 8-fold site. We emphasize that, qualitatively, our finding of elevated pyroxene/melt partition coefficients for heavy REE remains robust even if mineral-melt pairs are randomly assigned within each of the three systems. We make the effort to identify equilibrium pairs in order to isolate and quantify the heavy REE enrichment in the pyroxenes to the maximum extent allowed by the data.

For 25 FM Na-salite and 44 BT hedenbergite grains, apparent D_{REE} values were calculated using LA-ICP-MS-determined concentrations of La, Ce, Pr, Nd, Sm, Tb and Dy (approximately 500 phonolite glasses in the case of the Fasnia and approximately 100 high-silica rhyolite glasses from the BT). Eu is omitted due its unconstrained oxidation state, and heavy REE (Ho – Lu) for the reasons outlined above. Equilibrium between the pyroxenes and the different glasses is evaluated by assuming that isovalent cations entering a single lattice site will always follow a parabolic distribution in log D_i vs. r_i, using equation (1) rewritten as:

$$[RT/(-4\pi N_A)] * [\ln(D_i/D_0)] = E_M[r_0/2*(r_i - r_0)^2 + 1/3*(r_i - r_0)^3] \quad (2)$$

If the data follow the parabolic function exactly, the result is a straight line with slope E_M (Fig. 5c). Using equation (2) with the selected REE^{3+} La to Dy, the pyroxene-glass pair with the best R^2 correlation coefficient for the linear regression represents the closest approach to equilibrium and yields pyroxene-melt partition coefficients. We applied a filter of R^2 >0.95 to 12,500 possible pyroxene-glass pairings from the FM and 6,400 pairs from the BT, yielding 300 and 220 near-equilibrium pairs respectively. This approach is more rigorous than simply using predicted absolute D values because the fit does not depend on knowing D_0 or r_0, and relies on multiple elements. For the 40 RT pyroxenes, partition coefficients were calculated using pyroxenes paired with equilibrium glasses identified by Streck and Grunder (1997) and re-analyzed for this study.

From equation (2), the resultant calculated $^{VIII}E^{3+}_{M2}$ values for the Na-salites are 113 - 240 GPa (ave. 177 GPa), for BT hedenbergites 306 - 387 GPa (ave. 339 GPa) and for the RT ferroaugites 249 to 358 GPa (ave. 296 GPa). Our estimates of $^{VIII}E^{3+}_{M2}$ for the BT and RT pyroxenes compare well with published values of 256 to 387 GPa (Hill et al., 2000; Lundstrom et al., 1998). Those for the FM Na-salites are lower due to the influence of Na, a result also found experimentally by Bennett et al. (2004).

Model curves fitted to the average pyroxene-glass partition coefficients for each of the three populations are plotted on Figure 7. Parameters for each model curve are given in Table 4. Temperatures are from the literature for each system: Fasnia, assumed similar to other Tenerife phonolites, 825°C (Andujar et al., 2008); RT, 800°C (Streck and Grunder, 1997); and BT at 700°C (Warshaw and Smith, 1988). Values for the other parameters used in the model curves are determined in a two-step approach. First, values for the eight-fold coordination LSM equation come from equilibrium pyroxene-glass pairs identified using LREE and MREE in equation (2). This results in eight-fold coordination model values of: $^{VIII}r_0$ = 1.06 Å, $^{VIII}D_0$ = 1.6, and $^{VIII}E^{3+}_{M2}$ = 177 GPa for Na-salite; $^{VIII}r_0$ = 1.055 Å, $^{VIII}D_0$ = 5.2, and $^{VIII}E^{3+}_{M2}$ = 296 GPa for RT hedenbergites; and $^{VIII}r_0$ = 1.055 Å, $^{VIII}D_0$ = 9, and $^{VIII}E^{3+}_{M2}$ = 339 GPa for BT hedenbergites. Then, plausible values are chosen for the six-fold coordination LSM equation to fit the cumulative (VIII-fold + VI-fold) curves through the data, i.e., the heavy REE. The value of $^{VI}r_0$ = 0.724 Å , 0.758 Å and 0.772 Å for FM, RT and BT pyroxenes, respectively, is derived from the combined effective ionic radius, or weighted average, of the Fe^{2+}, Fe^{3+}, Mn, and Mg contents, and allows the model to be reasonably fitted through the D_{HREE} and the notably high D_{Sc} values for RT hedenbergites. For FM Na-salites $^{VI}D_0$ = 500 and $^{VI}E^{3+}_{M}$ = 775 GPa, for RT hedenbergites $^{VI}D_0$ = 150 and $^{VI}E^{3+}_{M}$ = 1000 GPa, and for BT hedenbergites $^{VI}D_0$ = 200 and $^{VI}E^{3+}_{M}$ = 1100 GPa. The $^{VI}E^{3+}_{M}$ values found here are comparable to values determined for diopside by Hill et al. (2000), Lundstrom et al. (1998) and Hazen & Finger (1979). It should be noted that $^{VI}D_0$ values are quite sensitive to small changes in $^{VI}r_0$ in the sixfold model equation. This is a function of the higher $^{VI}E_M$ values for this coordination state (Hill et al., 2000).

Immediately apparent from this exercise is that the negative D_Y anomaly seen in FM, RT, BT, and other iron-rich pyroxenes (Figs. 1,7) is not explained by the LSM, which predicts a smooth pattern across Dy, Y and Ho. This feature is discussed below.

Trace element partition coefficients

Each of the three Fe-rich clinopyroxene populations studied here exhibits a significant range in D_{REE}, (Figs. 6 – 9; Table 5). Na-salites have the following ranges in D-values for selected REE and Y (YREE): D_{La} 0.4 to 1.1 (aver. 0.6), D_{Sm} 1.0 to 2.4 (aver. 1.5), D_{Lu} 3.5 to 5.9 (aver. 4.5), and D_Y 0.9 to 1.8 (aver. 1.3). RT hedenbergites have D_{La} 0.7 to 1.2 (aver. 1.0), D_{Sm} 2.9 to 6.6 (aver. 5.0), D_{Lu} 4.0 to 7.9 (aver. 6.0), and D_Y 2.1 to 4.8 (aver. 3.7). BT hedenbergites have D_{La} 0.9 to 2.3 (aver. 1.2), D_{Sm} 6.3 to 15 (aver. 8.0), D_{Lu} 7.1 to 14 (aver. 10), and D_Y 3.8 to 7.2 (aver. 4.8). D_{REE} are positively correlated with each other as indicated by the uniform increase of D-values in Figure 5. In general, and especially in ferrohedenbergites from the BT, Y is less compatible into pyroxene than heavy REE of similar radius (Figs. 7, 8); this behavior is discussed below. Calculated D values for LREE and MREE are generally comparable to published values from a range of magma compositions (e.g., Sisson, 1991; Hart and Dunn, 1993; Schosnig and Hoffer, 1998; Hill et al., 2000; Bennett et al., 2004; Huang et al., 2006; Lofgren et al., 2006), but values for heavy REE are significantly higher relative to middle REE. Comparison of FM and RT pyroxenes shows that D_{Lu} increases with increasing Fe^{2+} and Mn contents. Among the RT hedenbergites, D_{Lu} is however negatively correlated with Fe contents, but positively correlated with Mn contents (Fig. 9).

Partition coefficients for HFSE are shown in Figure 8 and Table 5. Na-salites have the following selected D_{HFSE}: D_{Ti} 0.8 to 1.9 (aver. 1.3), D_{Zr} 0.7 to 1.7 (aver. 1.2), and D_{Hf} 1.0 to 2.8 (aver. 1.8). RT hedenbergites have D_{Ti} 1.2 to 2.0 (aver. 1.5), D_{Zr} 0.16 to 0.26 (aver. 0.21), and D_{Hf} 0.22 to 0.37 (aver. 0.28). BT hedenbergites have D_{Ti} 1.3 to 2.0 (aver. 1.6), D_{Zr} 0.17 to 0.40 (aver. 0.26), and D_{Hf} 0.27 to 0.98 (aver. 0.44). In all pyroxenes studied $D_{Hf} > D_{Zr}$ and $D_{Ho} > D_Y$, and in the Na-salites $D_{Ta} > D_{Nb}$ (Ta contents in BT and RT pyroxenes were below detection limits). Calculated HFSE partition coefficients are generally comparable to other published values (e.g., Sisson, 1991; Hart and Dunn, 1993; Schosnig and Hoffer, 1998; Hill et al., 2000; Bennett et al., 2004; Marks et al., 2004; Huang et al., 2006; Lofgren et al., 2006).

Discussion

Factors controlling HREE enrichment in pyroxene

The primary factors controlling the style of trace element partitioning between clinopyroxene and silicate melt are mineral composition and the ionic radius of the substituting cation. The generally lower $^{VIII}E^{3+}$ values for Na-salites relative to the ferrohedenbergites and ferroaugites is attributed to their higher Na contents ; Na cations have the effect of opening the calcic pyroxene structure and lowering $^{VIII}E^{3+}$ (Bennett et al., 2004).

We have shown that the HREE enrichment of these pyroxenes is plausibly explained by their high Fe contents (i.e., Fe^{2+}) that are common to all three groups studied here, but variations in D_{HREE} within the FM and RT pyroxene populations are not apparently controlled by Fe contents alone (Fig. 9); considering the RT pyroxenes in isolation, D_{Lu} is strongly positively correlated with Mn contents, but negatively correlated with Fe contents. This suggests that Mn, in fact, has a more powerful effect than Fe^{2+} in creating the space for 6-fold coordinated heavy REE to substitute into the pyroxene structure. This is consistent with Mn having the larger ionic radius.

Fractionation of Y/Ho, Zr/Hf, and Nb/Ta

The elements in each of these pairs have closely similar radii and have been viewed in the past as chemically identical at magmatic temperatures. Thus, Y was commonly used as a proxy for the HREE between Tb and Yb prior to the routine availability of high-quality ICPMS data for all 14 REE (for example, Thompson et al., 1984). Significant fractionation in these pairs of elements is observed at sub-magmatic temperatures (Bau, 1996, 1999; Bau and Dulski, 1999) and, in plutonic rocks, has been ascribed to the action of aqueous fluids during the final stages of crystallization (Irber, 1999). Carbonatite liquids have also been implicated in Zr/Hf and Nb/Ta fractionation (Rudnik et al., 1993). Nonetheless, it is now well established that these element pairs are fractionated during common crystallization-differentiation processes. Magmatic fractionation of Nb from Ta was first demonstrated by Wolff (1984) in Tenerife phonolites and shown to be due to titanite crystallization; Ti-rich phases in general have high *D* values for HFSE and are effective in separating these two elements (Green and Pearson, 1986). The restricted *P-T-X* conditions under which phases such as titanite and rutile are stable has lead to considerable attention being paid to variations in Nb/Ta, in particular, among different terrestrial reservoirs (Rudnik et al., 1993; Collerson et al., 2007; Horng and Hess, 2000; Wade and Wood, 2001; Foley et al., 2002). With the advent of high-quality mineral-melt partitioning data, it has become clear that common phases such as clinopyroxene and amphibole also fractionate Y from Ho, Zr from Hf, and Nb from Ta (Lundstrom et al., 1998; Tiepolo et al., 2002).

The ability of the LSM to predict these fractionations depends on accurate ionic radius data. Nb^{5+} and Ta^{5+} are conventionally viewed as having identical radii, Zr^{4+} and Hf^{4+} are slightly different, while the radius of Y^{3+} lies between those of Dy^{3+} and Ho^{3+} in eight-fold coordination, but is nearly identical to Ho^{3+} in 6-fold coordination (Shannon 1976; relevant values are reproduced in Table 3. Note that in the older compilation of Whittaker & Muntus, 1970, the ionic radii of Y^{3+} and Ho^{3+} are equal in both 6-fold and 8-fold coordination). Accuracy of the LSM is difficult to assess for Nb-Ta and Zr-Hf, because the very high *E* values associated with high valencies and the small M1 site in clinopyroxene imply easily detectable changes in *D* at variations in $r \leq 0.01$ Å, beyond the resolution of the Shannon (1976) ionic radius data. Blundy and Wood (2003) in fact propose that the ionic radius of Ta^{5+} is 0.01 – 0.02 Å smaller that that of Nb^{5+}, based on D_{Nb}/D_{Ta} variations in Ti-pargasite and kaersutite documented by Tiepolo et al. (2002). However, inspection of Figure 7 shows that Y^{3+} cpx/melt partitioning deviates from that of the HREE to an extent that the LSM cannot explain unless the Shannon (1976) value of the ionic radius for Y^{3+} is grossly in error, and really lies within the range of ionic radii of the light REE! Titanite displays similar behavior to a greater degree (Olin, 2007). This result is not entirely unexpected; there can be little doubt that ionic radius and charge are more important than other factors in predicting D values, and so the effects of deviations from the LSM should be most apparent among isovalent cations of similar radii. Although small differences in ionic radius may indeed cause fractionation of Nb from Ta and Zr from Hf, this cannot explain the fractionation of Y from the heavy REE. The pairs Y-Ho, Zr-Hf and Nb-Ta share a common

feature, which is that the lighter cation has the outer electronic configuration [Kr], and the heavier cation has buried 4*f* electrons and the outer electronic configuration [Xe]. Contrasts in behavior between the members of each pair may therefore be due to electronic effects, such as the related properties of electronegativity and ionic polarizability, and/or mass effects.

Sources of deviation from the LSM

The LSM assumes that cations behave as 'billiard balls' with evenly distributed surface charge. Deviations are expected where outer electronic structure cannot be so modeled, for example crystal field effects resulting from the involvement of *d* orbitals in bonding, or the presence of a lone pair of electrons (Blundy and Wood, 1994). The ions Y^{3+}, Ho^{3+}, Zr^{4+}, Hf^{4+}, Nb^{5+} and Ta^{5+} all have inert gas outer electronic configurations and therefore approximate to charged billiard balls, but exhibit variation in electronegativity and ionic polarizability (Table 6), i.e. the tendency to develop uneven charge distribution.

Horng and Hess (2002) invoked the polarizability difference of Nb_2O_5 and Ta_2O_5 (as a proxy for NbO_6 and TaO_6 octahedra in minerals and melts), calculated from specific refractivity values tabulated by Jaffe (1988), to explain experimentally-determined fractionation of Nb/Ta between rutile and haplogranite melt. Using the same tabulation (Table 6), polarization effects are predicted to operate in one sense for Y-HREE and Zr-Hf, and in the opposite sense for Nb-Ta. Using the more recent compilation of ionic polarizabilities of Shannon and Fischer (2006), dipole effects for Y-HREE should act in the opposite sense to Zr-Hf and Nb-Ta (Table 6). The differences in electronegativity and polarizability between Y and HREE are also small. Although not consistent in the prediction of Zr-Hf behavior, both approaches predict opposite senses of Y-Ho and Nb-Ta partitioning. This contrasts with our data, which shows that the heavy element in each pair is always the more compatible. With the understanding that as yet undetected differences in ionic radius may trump secondary effects, we briefly speculate on the possible role of mass effects.

Mass fractionation effects?

By analogy with the theoretical treatment of stable isotope fractionation (Chacko et al., 2001), mass fractionation between two otherwise identical ions may be crudely approximated by treating the metal-oxide bond as a diatomic molecule that behaves as a simple harmonic oscillator (spring) connecting two masses m_M and m_O, where M and O denote the metal and oxygen respectively. The vibrational frequency, ν, of the oscillator is given by

$$\nu = (k/\mu)^{0.5}/2\pi \qquad (3)$$

□□□□□□k is the force constant of the spring (a property related to the elastic modulus), and μ is the reduced mass, given by $\mu = m_M m_O/(m_M + m_O)$. In this model, a strong chemical bond can be thought of as a spring with a high force constant, resulting in a higher vibrational frequency. From equation (3), changing the mass of the metal ion gives

$$\nu^*/\nu = (\mu/\mu^*)^{0.5} \qquad (4)$$

where the asterisk denotes substitution of the heavier atom. Due to the inverse relation between frequency and mass, the heavy molecule has a lower vibrational frequency than the lighter molecule and hence is more energetically stable. Partitioning between two phases then depends on their competition for the heavy atom. Equation (4) can be rearranged to yield

$$\nu - \nu^* = \nu[1 - (\mu/\mu^*)^{0.5}] \qquad (5)$$

from which it can be seen that the heavy atom favors the phase with stronger M-O bonds (higher ν).

Because we have no information on the strengths of trace metal – oxygen bonds in silicate liquids, we cannot make quantitative estimates of pyroxene-melt mass fractionation effects for trace elements. Nonetheless, some qualitative predictions are possible based on equations (3) – (5). First, the sign of

heavy/light partitioning should always be the same for any given phase/melt pair, i.e., either the heavy or the light element should prefer the solid phase for each of the pairs Y-Ho, Zr-Hf, and Nb-Ta. Second, we expect that the mineral phase will in most cases favor the heavy element in each pair. This is because M-O bonds in silicate liquids are assumed to be considerably weaker than the same bonds in solid phases; the very success of the LSM, which ignores melt structural effects, in predicting first-order partitioning behavior supports this assumption. Our data, plus a review of the literature for pyroxene-melt, amphibole-melt, titanite-melt, rutile-melt, magnetite-melt, and ilmenite-melt partitioning of Y/Ho, Zr/Hf and Nb/Ta reveals that in each case the partition coefficients are higher for the heavier elements (e.g., Stimac and Hickmott, 1994; Bottazzi et al., 1999; Oberti et al., 2000; Horng and Hess, 2000; Nielsen and Beard, 2000; Tiepolo et al., 2002; Prowatke and Klemme, 2005). This would be a remarkable coincidence if small differences in radii were solely responsible, given the variety of phases and lattice sites represented. Third, the discrepancy between partitioning behavior of the heavy and light element in each pair should increase with ionic charge. This is because $(n - n^*)/n$ values (eqn. 5) are approximately constant (0.0365 ± 0.007) for each of the three element pairs, but M-O bond strength is expected to increase with increasing charge on M, all else equal, and so the mass fractionation effect should be enhanced. This effect is seen in our data (Fig. 8). Finally, mass fractionation effects are expected to be inversely correlated with temperature. This effect is also seen in our data (Figure 8), for which $T_{\mathrm{Fasnia}} > T_{\mathrm{RT}} > T_{\mathrm{BT}}$.

Niu & Hékinian (1997) and Niu (2004) also appealed to mass-dependent fractionation as a possible explanation for large variations in Zr/Hf and Nb/Ta among abyssal peridotites, and noted that kinetic effects enhance mass fractionation because diffusion coefficients are themselves mass dependent. It is possible that, at the relatively low magmatic temperatures of the systems investigated here, chemical kinetics could play a detectable role in cation partitioning between pyroxene and melt, and may be more marked than equilibrium mass fractionation effects. Variable Y/Ho, Zr/Hf and Nb/Ta remains an intriguing problem in igneous geochemistry that awaits a fundamental explanation.

Conclusions

Heavy REE enrichment in Fe-rich clinopyroxenes from felsic magmas is caused by substitution into 6-coordinated sites (M2 or M1). Increased heavy REE compatibility coincides with the higher Fe and Mn contents of these pyroxenes relative to more magnesian pyroxenes described elsewhere. This behavior can be modeled by summing the results for the two lattice strain model equations for 6-fold and 8-fold coordinated 3+ cations with reasonable parameter values. Fractionation of Y from REE is observed in all three systems studied here and is not predicted by the lattice strain model. This feature cannot be explained by cation size differences, and may instead be a consequence of electronic effects or, as we speculate here, mass-dependent fractionation. If so, the same effect(s) may possibly play a role in the fractionation of Zr from Hf, and of Nb from Ta.

Acknowledgements

We would like to acknowledge Charles Knaack and Scott Cornelius of the Washington State University GeoAnalytical Laboratory for their assistance with ICP-MS and electron microprobe data collection. Early discussions with Else-Ragnhild Neumann were instrumental in initiating this study. We also thank Martin Streck for contributing Rattlesnake Tuff pyroxenes and glasses to this study. Fieldwork on Tenerife was funded by NSF grant EAR-0001013, and in the Jemez Mountains by NSF EAR-9909700.

References

Andujar J, Costa F, Martí J, Wolff JA, Carroll MR (2008) Experimental constraints on pre-eruptive conditions of phonolitic magma from the caldera-forming El Abrigo eruption, Tenerife (Canary Islands). Chem Geol 257: 173-191

Bau M (1999) Scavenging of dissolved yttrium and rare earths by precipitating iron oxyhydroxide: Experimental evidence for Ce oxidation, Y-Ho fractionation, and lanthanide tetrad effect. Geochim Cosmochim Acta 63: 67-77

Bau M (1996) Controls on the fractionation of isovalent trace elements in magmatic and aqueous systes: evidence from Y/Ho, Zr/Hf, and lanthanide tetrad effect. Contrib Mineral Petrol 123: 323-333

Bau M, Dulski P (1999) Comparing yttrium and rare earths in hydrothermal fluids from the Mid-Atlantic Ridge: implications for Y and REE behaviour during near-vent mixing and for the Y/Ho ratio of Proterozoic seawater. Chem Geol 155: 77-90

Bennett SL, Blundy J, Elliott T (2004) The effect of sodium and titanium on crystal-melt partitioning of trace elements. Geochim Cosmochim Acta 68: 2335-2347

Blundy J, Wood B (2003) Partitioning of trace elements between crystals and melts. Earth Planet Sci Lett 210: 383-397

Blundy JD, Robinson JAC, Wood BJ (1998) Heavy REE are compatible in clinopyroxene on the spinel lherzolite solidus. Earth Planet Sci Lett 160: 493-504

Blundy J, Wood B (1994) Prediction of crystal-melt partition coefficients from elastic moduli. Nature 372: 452-454

Bottazzi P, Tiepolo M, Vannucci R, Zanetti A, Brumm R, Foley SF, Oberti R (1999) Distinct site preferences for heavy and light REE in amphibole and the prediction of $^{Amph/L}D_{REE}$. Contrib Mineral Petrol 137: 36-45

Brice JC (1975) Some thermodynamic aspects of the growth of strained crystals. J Cryst Growth 28: 249-253

Cameron M, Papike JJ (1980) Crystal chemistry of silicate pyroxenes. Reviews in Mineralogy 7: 5-92

Chacko T, Cole DR, Horita J (2001) Equilibrium oxygen, hydrogen and carbon isotope fractionation factors applicable to geologic systems. Reviews in Mineralogy and Geochemistry 43: 1-81

Collerson KD, Williams Q, Murphy D (2007) Chemical and isotopic heterogeneities in the deep Earth; importance of lower mantle carbonate-rich melts. Eos Trans AGU 88: 52 Suppl

Droop GTR (1987) A general equation for estimating Fe^{3+} concentrations in ferromagnesian silicates and oxides from microprobe analyses, using stoichiometric criteria. Mineral Mag 51: 431-435

Edgar C, Wolff JA, Olin PH, Nichols, HJ, Pitarri A, Cas RAF, Reiners PW, Spell TL, Martí J (2007) The late Quaternary Diego Hernandez Formation, Tenerife: a cycle of repeated voluminous explosive phonolitic eruptions. J Volcanol Geotherm Res 160: 59-85

Fedele L, Zanetti A, Vincenzo M, Lustrino M, Melluso L, Vannucci R (2009) Clinopyroxene/liquid trace element partitioning in natural trachyte-trachyphonolite systems: insights from Campi Flegrei (southern Italy). Contrib Mineral Petrol (doi:10.1007/s00410-009-0386-5)

Foley SF, Tiepolo M, Vannucci R (2002) Trace element partitioning evidence for growth of early continental crust from amphibolites, not eclogites. Geochim Cosmochim Acta 66: 238

Gaetani GA, Grove TL (1995) Partitioning of rare earth elements between clinopyroxene and silicate melt; crystal chemical controls. Geochim Cosmochim Acta 59: 1951-1962

Green TH, Pearson NJ (1987) An experimental study of Nb and Ta partitioning between Ti-rich minerals and silicate liquids at high pressure and temperature. Geochim Cosmochim Acta 51: 55-62

Hamilton DL, MacKenzie WS (1965) Phase-equilibrium studies in the system $NaAlSiO_4$ (nepheline) – $KalSiO_4$ (kalsilite) – SiO_2 – H_2O. Mineral Mag 34: 214-231

Hart SR, Dunn T (1993) Experimental cpx/melt partitioning of 24 trace elements. Contrib Mineral Petrol 113: 1-8

Hauri EH, Wagner TP, Grove TL (1994) Experimental and natural partitioning of Th, U, Pb and other trace elements between garnet, clinopyroxene and basaltic melts. Chem Geol 117: 149-166

Hazen RM, Finger LW (1979) Bulk modulus-volume relationship for cation-anion polyhedra. J Geophys Res 84: 6723-6728

Hill E, Wood B, Blundy J (2000) The effect of Ca-Tschermaks component on trace element partitioning between clinopyroxene and silicate melt. Lithos 53: 203-215

Horng W, Hess PC (2000) Partition coefficients of Nb and Ta between rutile and anhydrous haplogranite melts. Contrib Mineral Petrol 138: 176-185

Huang F, Lundstrom CC, McDonough WF (2006) Effect of the melt structure on trace-element partitioning between clinopyroxene and silicic, alkaline, aluminous melts. Am Mineral 91: 1385-1400

Irber W (1999) The lanthanide tetrad effect and its correlation with K/Rb, Eu/Eu*, Sr/Eu, Y/Ho, and Zr/Hf of evolving peraluminous granite suites. Geochim Cosmochim Acta 63: 489-508

Jaffe HW (1988) Crystal chemistry and refractivity. Cambridge University Press, Cambridge, p.118-140

Kuentz DC (1986) The Otowi Member of the Bandelier Tuff; a study of the petrology, petrography, and geochemistry of an explosive silicic eruption, Jemez Mountains, New Mexico. MSc thesis, University of Texas Arlington, USA.

Larsen LM (1979) Distribution of REE and other trace elements between phenocrysts and peralkaline undersaturated magmas, exemplified by rocks from the Gardar igneous province, south Greenland. Lithos 12: 303-315

Lofgren GE, Huss GR, Wasserburg GJ (2006) An experimental study of trace-element partitioning between Ti-Al-clinopyroxene and melt: Equilibrium and kinetic effects including sector zoning. Am Mineral 91: 1596-1606

Lundstrom CC, Shaw HF, Ryerson FJ, Williams Q, Gill J (1998) Crystal chemical control of clinopyroxene-melt partitioning in the Di-Ab-An system: implications for elemental fractionations in the depleted mantle. Geochim Cosmochim Acta 62: 2849-2862.

Mahood GA, Stimac JA (1990) Trace-element partitioning in pantellerites and trachytes. Geochim Cosmochim Acta 54: 2275-2276

Min K, Reiners PW, Wolff JA, Mundil R, Winters RL (2006) (U-Th)/He dating of volcanic phenocrysts with high-U,Th inclusions, Bandelier Tuff, New Mexico. Chem Geol 227: 223-235

Nash WP, Crecraft HR (1985) Partition coefficients for trace elements in silicic magmas. Geochim Cosmochim Acta 49: 2309-2322

Niu Y (2004) Bulk-rock major and trace element compositions of abyssal peridotites: implications for mantle melting, melt extraction and post-melting processes beneath mid-ocean ridges. J Petrol 45: 2423-2458

Niu Y, Hékinian R (1997) Basaltic liquids and harzburgitic residues in the Garrett Transform: a case study at fast-spreading ridges. Earth Planet Sci Lett 146: 243-258

Nielsen RL, Beard JS (2000) Magnetite-melt partitioning. Chem Geol 164: 21-34

Oberti R, Vannucci R, Zanetti A, Tiepolo M, Brumm RC (2000) A crystal chemical re-evaluation of amphibole/melt and amphibole/clinopyroxene D_{Ti} values in petrogenetic studies. Am Min 85: 407-419

Olin PH (2007) Magma dynamics of the Diego Hernández Formation, Tenerife, Canary Islands. PhD thesis, Washington State Univ, USA, 416 pp.

Perterman M, Hirschmann MM (2002) Trace element partitioning between vacancy-rich clinopyroxene and silicate melts. Am Mineral 87: 1365-1376

Poldervaart A, Hess HH (1951) Pyroxenes in the crystallization of basaltic magma. J Geology 59: 472-489

Prowatke S, Klemme S (2005) Effect of melt composition on the partitioning of trace elements between titanite and silicate melt. Geochim Cosmochim Acta 69: 695-709

Robinson P (1980) The composition space of terrestrial pyroxenes – internal and external limits. Reviews in Mineralogy 7: 419-494

Rudnick RL, McDonough WF, Chappell BW (1993) Carbonatite metasomatism in the northern Tanzanian mantle; petrographic and geochemical characteristics. Earth Planet Sci Lett 114: 463-475

Schosnig M, Hoffer E (1998) Compositional dependence of REE partitioning between diopside and melt at 1 atmosphere. Contrib Mineral Petrol 133: 205-216

Shannon RD (1976) Revised effective ionic radii and systematic studies of interatomic distances in halides and chalcogenides. Acta Crystallogr A 32: 751-767

Shannon RD, Fischer RX (2006) Empirical electronic polarizabilities in oxides, hydroxides, oxyfluorides, and oxychlorides. Phys Rev B 73: 235111

Sisson TW (1991) Pyroxene-high silica rhyolites trace element partition coefficients measured by ion microprobe. Geochim Cosmochim Acta 55: 1575-1585

Spell TL, Kyle PR, Thirwall MF, Campbell AR (1990) Nd, Sr, and O isotopic geochemistry of postcollapse rhyolites in the Valles Caldera, New Mexico. Eos Trans AGU 71: 1676

Streck MJ, Grunder AL (1997) Compositional gradients and gaps in high-silica rhyolites of the Rattlesnake Tuff, Oregon. J Petrol 38: 133-163

Streck MJ, Grunder AL (2007) Phenocryst-poor rhyolites of bimodal, tholeiitic provinces: the Rattlesnake Tuff and implications for mush extraction models. Bull Volcanol 70: 385-401

Stimac J, Hickmott D (1994) Trace-element partition coefficients for ilmenite, orthopyroxene and pyrrhotite in rhyolite determined by micro-PIXE analysis. Chem Geol 117: 313-330

Thompson RN, Morrison MA, Hendry GL, Parry SJ (1984) An assessment of the relative roles of crust and mantle in magma genesis: an elemental approach. Phil Trans R Soc London A 310: 549-590

Tiepolo M, Oberti R, Vannucci R (2002) Trace-element incorporation in titanite: constraints from experimentally determined solid/liquid partition coefficients. Chem Geol 191: 105-119

Tuttle OF, Bowen NL (1958) Origin of granite in the light of experimental studies in the system NaAlSi3O8-KAlSi3O8-SiO2-H2O. Geol Soc Amer Memoir 74.

Vannucci R, Bottazzi P, Wulff-Pedersen E, Neumann E-R (1998) Partitioning of REE, Y, Sr, Zr and Ti between clinopyroxene and silicate melts in the mantle under La Palma (Canary Islands): implications for the nature of the metasomatic agents. Earth Planet Sci Lett 158: 39-51

Wade J, Wood BJ (2001) The Earth's 'missing' Nb may be in the core. Nature 409: 75-78

Warshaw CM, Smith RL (1988) Pyroxenes and fayalites in the Bandelier Tuff, New Mexico: Temperatures and comparisons with other rhyolites. Am Mineral 73: 1025-1037

Wolff JA (1984) Variation in Nb/Ta during differentiation of phonolitic magma, Tenerife, Canary Islands. Geochim Cosmochim Acta 48: 1345-1348

Wolff JA, Grandy JS, Larson PB (2000) Interaction of mantle-derived magma with island crust? Trace element and oxygen isotope data from the Diego Hernandez Formation, Las Cañadas, Tenerife. J Volcanol Geotherm Res 103: 343-366

Wolff JA, Ramos FC, Davidson JP (1999) Sr isotope disequilibrium during differentiation of the Bandelier Tuff; constraints on the crystallization of a large rhyolitic magma chamber. Geology 27: 495-498

Wolff JA, Storey M (1984) Zoning in highly alkaline magma bodies. Geol Mag 121: 563-575

Wolff JA, Storey M (1983) The volatile component of some pumice-forming alkaline magmas from the Azores and Canary Islands. Contrib Mineral Petrol 82: 66-74

Wood BJ, Blundy JD (2002) The effect of H2O on crystal-melt partitioning of trace elements. Geochim Cosmochim Acta 66: 3647-3656

Wood B, Blundy J (2001) The effect of cation charge on crystal-melt partitioning of trace elements. Earth Planet Sci Lett 188: 59-71

Wood B, Blundy J (1997) A predictive model for rare earth element partitioning between clinopyroxene and anhydrous silicate melt. Contrib Mineral Petrol 129: 166-181

Wood B, Trigila R (2001) Experimental determination of aluminous clinopyoxene-melt partition coefficients for potassic liquids, with application to the evolution of the Roman province potassic magmas. Chem Geol 172: 213-223

Wörner G, Beusen JM, Duchateau N, Gijbels R, Schmincke H-U (1983) Trace element abundances and mineral/melt distribution coefficients in phonolites from the Laacher See Volcano (Germany). Contrib Mineral Petrol 84: 152-173

Figure captions

Figure 1: Clinopyroxene-melt REE partition coefficients versus atomic number of pyroxenes from the literature and from this study. Literature data are from pyroxenes in alkali basalt (Hart and Dunn, 1993; Mg# 55.2; black triangles), lherzolite (Blundy et al., 1998; Mg# 83.7; black diamonds), phonolite (Wörner et al., 1983; Mg# 65.6; black circles), phonolite (Larsen, 1979; Mg# 25.3; black squares), pantellerite (Mahood and Stimac, 1990; Mg# 18.3; open triangles), trachyphonolite (Fedele et al., 2009; Mg# 67; open circles), high-silica rhyolite (Sisson, 1991; Mg# 16.8; open squares), rhyolite (Nash and Crecraft, 1985; Mg# 41.7; dashed x). Data from this study; average Na-salite in Fasnia Member phonolite (Mg# 48 to 59; red), average ferroaugite/ferrohedenbergite in Rattlesnake Tuff rhyolite (Mg# 9.6 to 32; solid black), average ferroaugite/ferrohedenbergite in Bandelier Tuff high-silica rhyolite (Mg# 14.2 to 16.2; blue).

Figure 2: Pyroxene quadrilateral showing Tenerife Na-salites (FM), Rattlesnake Tuff (RT) ferrohedenbergites to ferroaugites, and Bandelier Tuff (BT) ferrohedenbergites. Pyroxene quadrilateral after Poldervaart and Hess, 1951.

Figure 3: Rare earth elements contents of average pyroxene (solid symbols) and glass (open symbols) compositions for FM (red), RT (black), and BT (blue) normalized to Bulk Silicate Earth, McDonough & Sun, 1995. For comparison, values determined for standard materials BCR (gray) and in-house pyroxene (TFPX, black) are also shown for laser ablation (solid, no symbols) and solution (dashed, no symbols) methods.

Figure 4: Covariations of selected minor and trace elements and ratios in the pyroxenes.

Figure 5: Lattice strain model plotted (a) as Log(partition coefficient) versus ionic radius for idealized elements of the same valence state and same coordination number, where D_0 is the partition coefficient for the optimal ionic radius r_0, and E_M is the Young's modulus for the site, (b) showing REE^{3+} partition coefficient distribution for six-fold and eight-fold coordination in pyroxene, and (c) shows equation (2), the linear expression of model equation. Samples shown in (c) have the best R^2 values from each of the three populations (FM red, RT black, BT blue), for elements La through Dy in eight-fold coordination (see text for details).

Figure 6: Calculated REE partition coefficient ranges for FM, RT, and BT pyroxenes.

Figure 7: Model curves for REE^{3+} cations for FM (a), RT (b), and BT (c) pyroxenes. The model curves are for elements in six-fold (red, squares) and eight-fold (blue, diamonds) coordination and the sum of the two curves (solid black, triangles). The average composition for each population is also shown (black dashed, gray x), but is obscured by the model curves. Note that the negative Y partition coefficient anomaly that is especially prominent in average RT and BT hedenbergites, and in other iron-rich pyroxenes in Figure 1, is not predicted by the model (see text for details).

Figure 8: Partition coefficient co-variation and ratio plots for selected trace elements.

Figure 9: D_{Lu} versus Fe^{2+} and Mn contents of the pyroxenes. BT samples are omitted from this plot because trace element analyses do not correspond to locations for major element determinations.

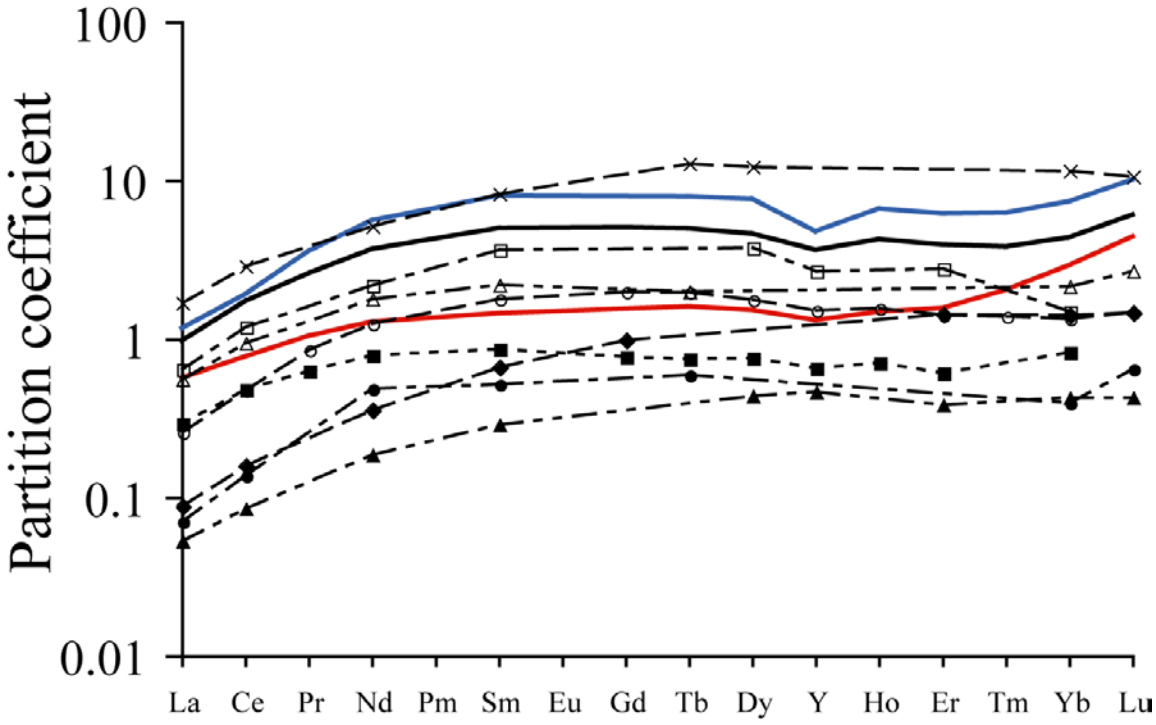

Figure 1

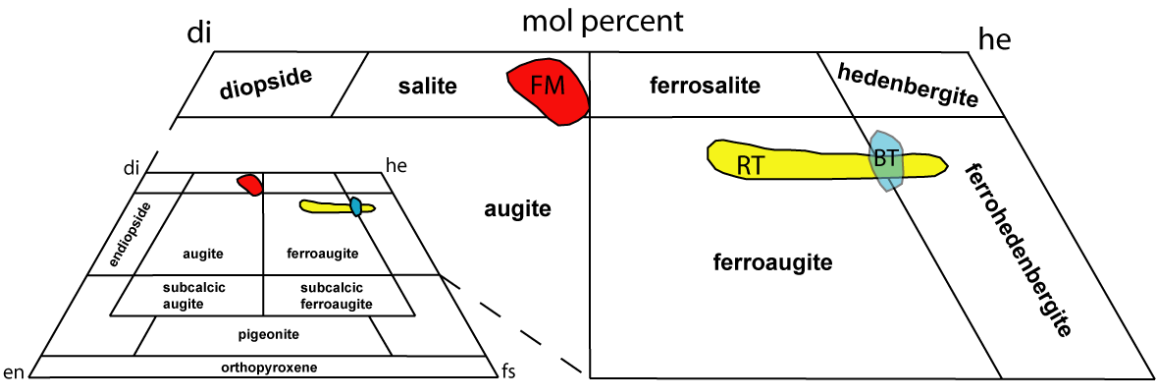

Figure 2

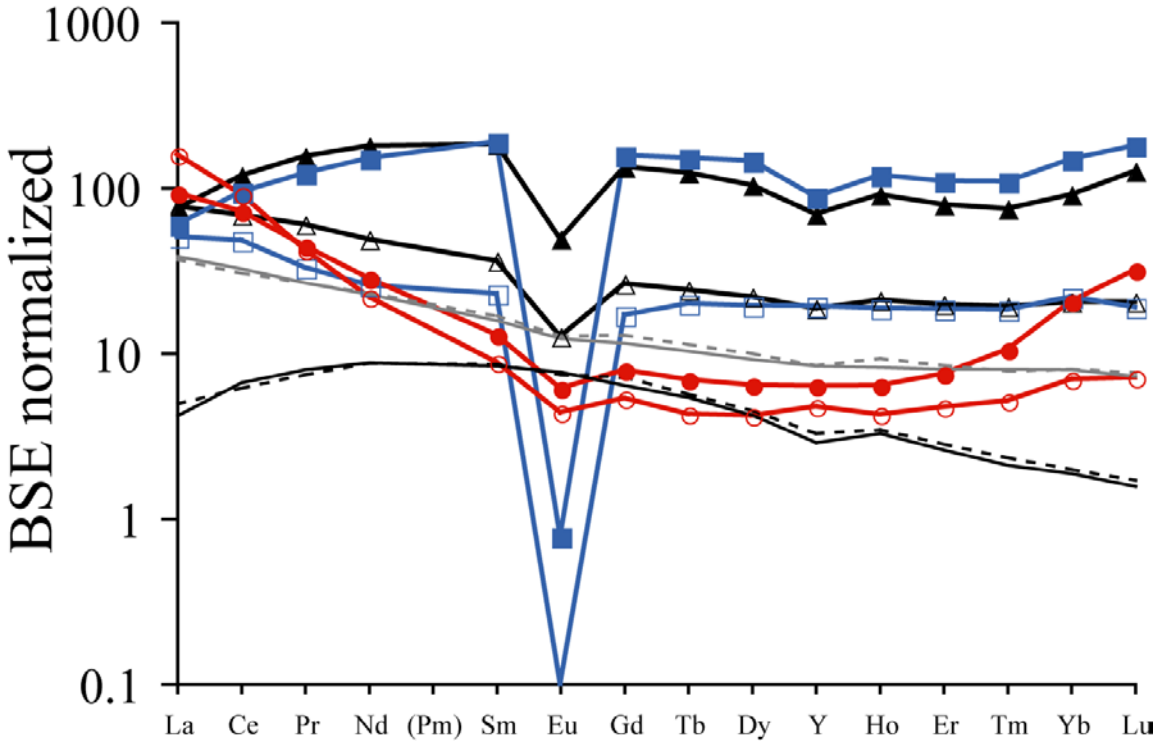

Figure 3

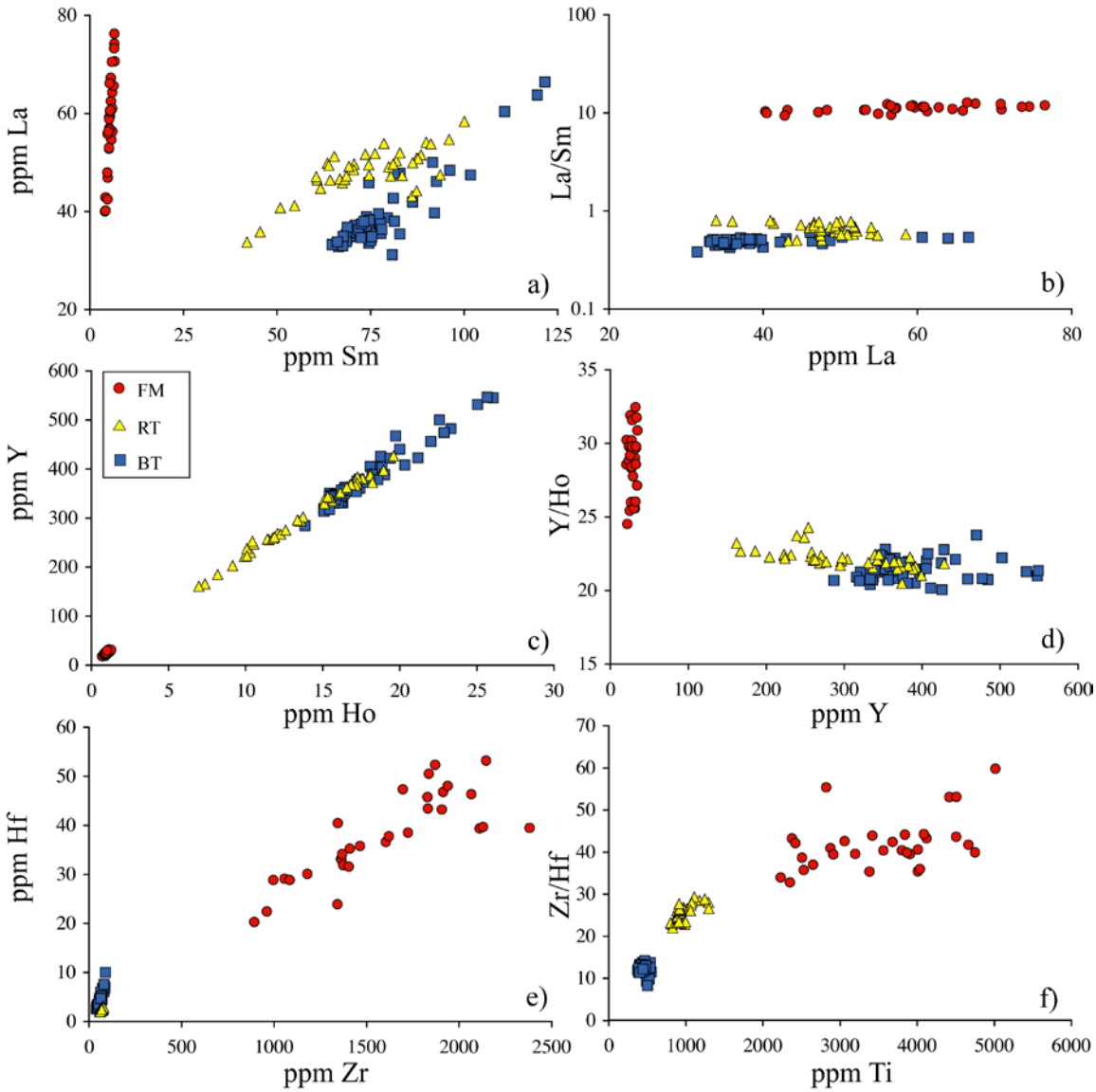

Figure 4

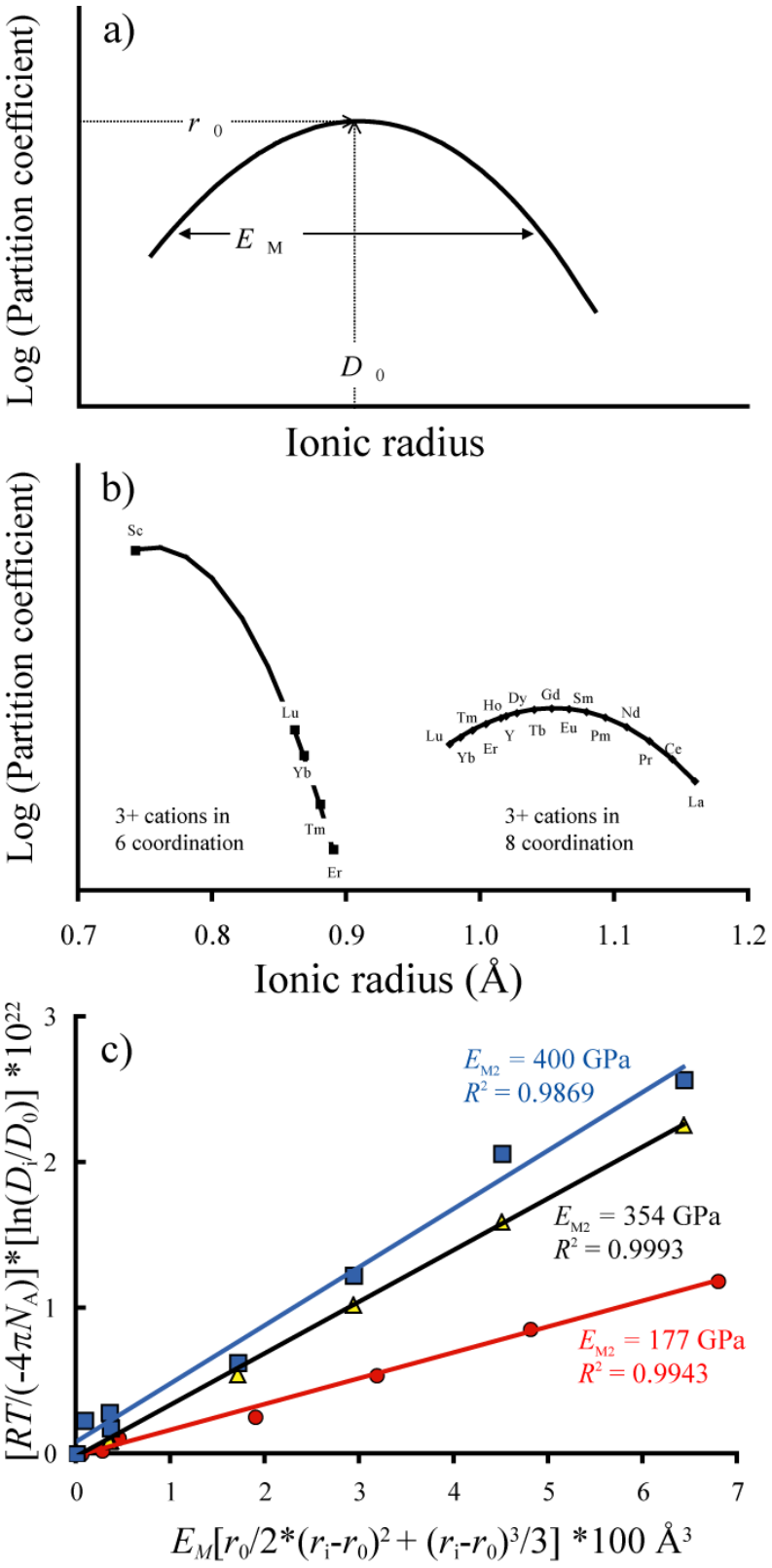

Figure 5

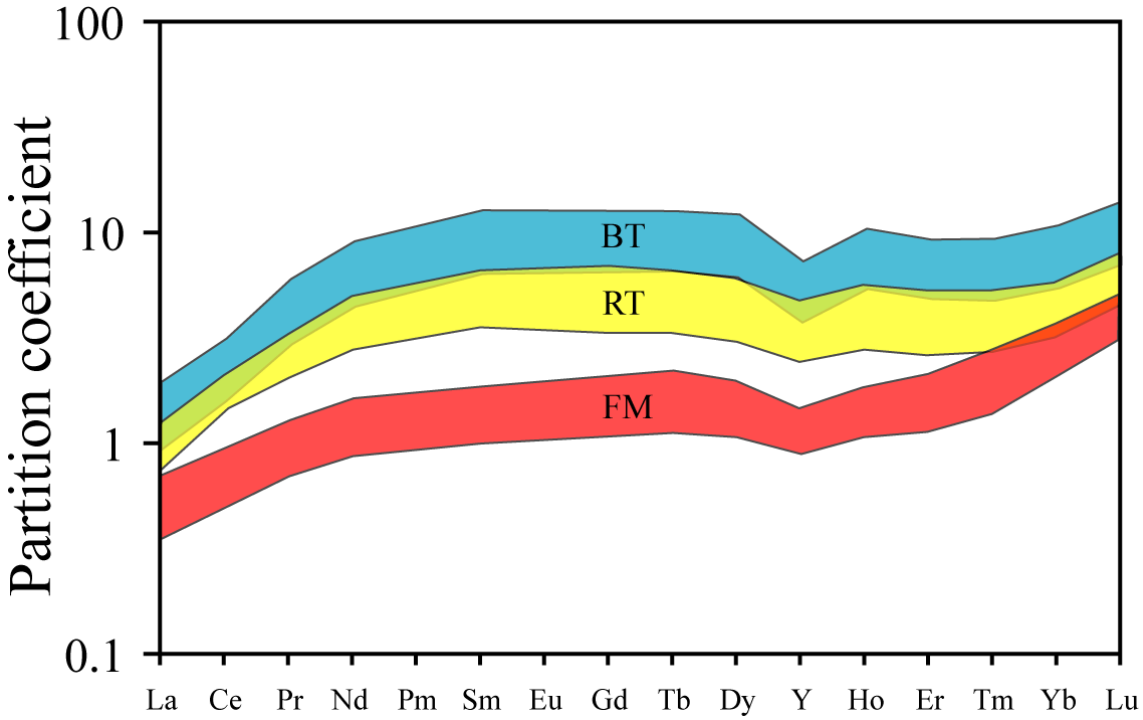

Figure 6

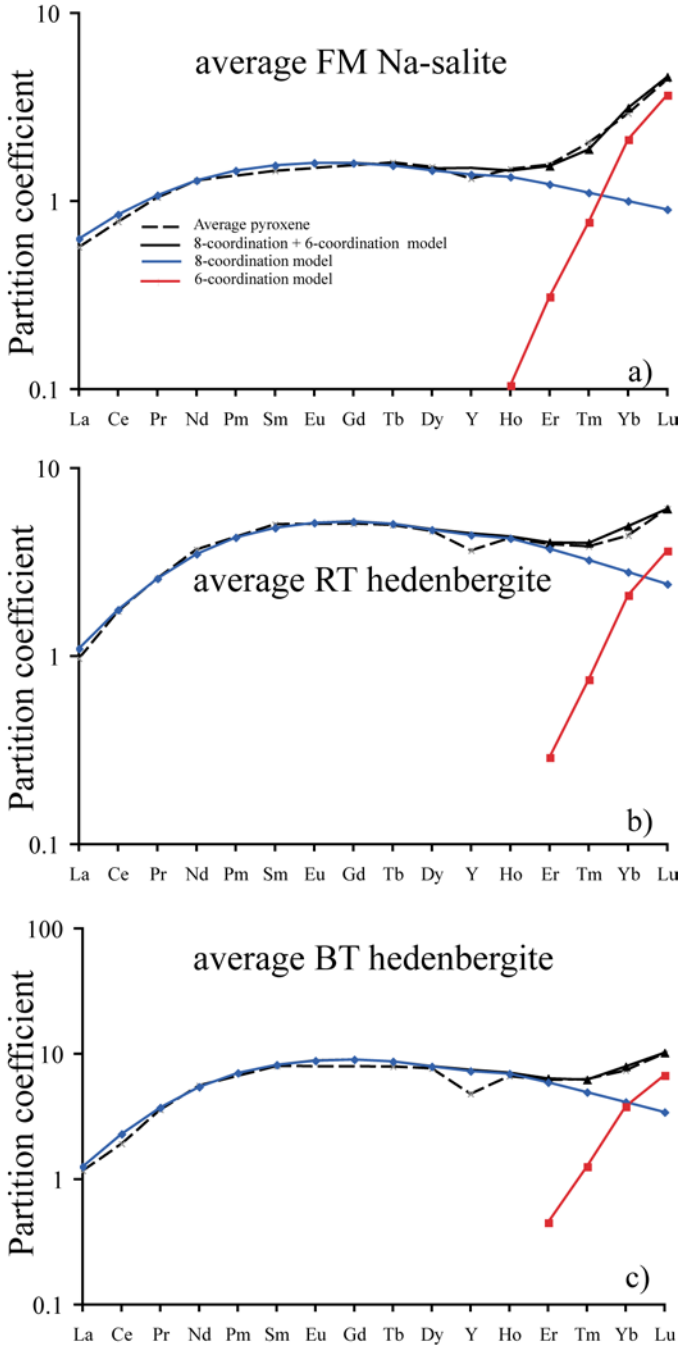

Figure 7

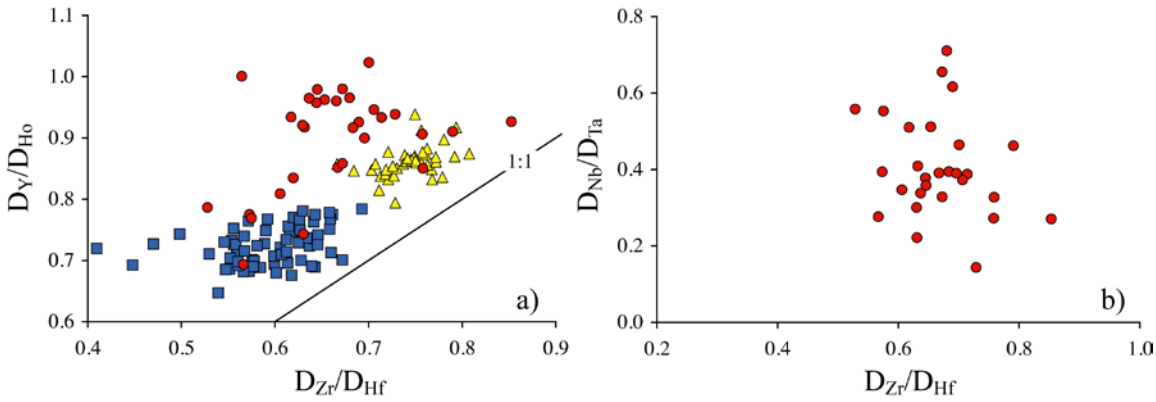

Figure 8

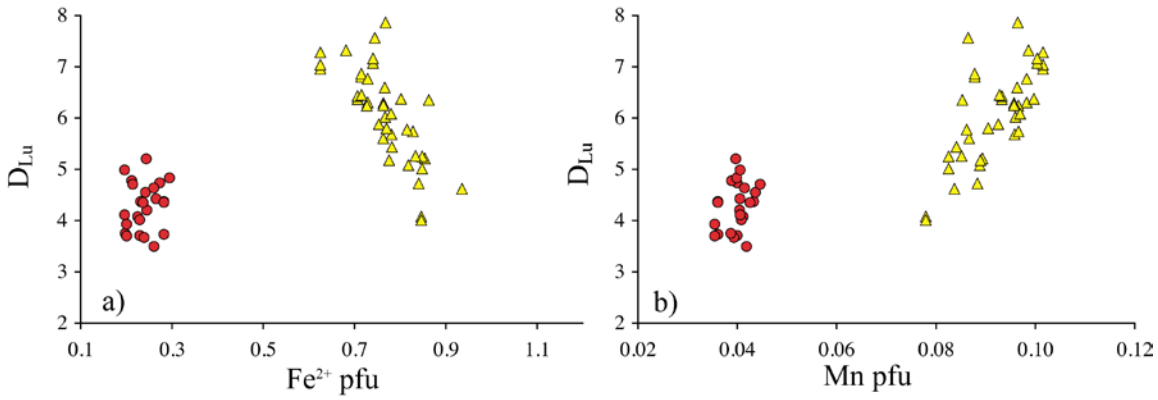

Figure 9

Table captions

Table 1. Characteristics of the three felsic volcanic units analyzed in this study.

Table 2: Representative major and trace element contents of FM, RT and BT pyroxenes and glasses. BT pyroxene major element and trace element values are from different grains.

Table 3: Ionic radii for major and trace element cations in eight- and six-fold coordination, from Shannon (1976).

Table 4: Values for lattice strain model parameters used to generate model curves in Figure 7.

Table 5: Pyroxene-glass partition coefficients; maximum, minimum, average, and model curve values.

Table 6: Electronic polarizability, α, of Y, HREE, and HFSE cations, from Shannon and Fischer (2006). $\Delta = [\alpha_{\text{(light ion)}} - \alpha_{\text{(heavy ion)}}]/\alpha_{\text{(light ion)}}$

Table 1

	Fasnia Member (FM)[1]	**Otowi Member of the Bandelier Tuff (BT)[2]**	**Rattlesnake Tuff (RT)[3]**
Volcano or province	Las Cañadas, Tenerife, Canary Islands, Spain	Valles caldera, New Mexico, USA	High Lava Plains, eastern Oregon, USA
Age, Ma	0.309	1.61	7.05
Magma volume, km^3	13	~120*	280
Magma composition	Minimum-melt phonolite	Minimum-melt high-silica rhyolite	Rhyolite, 75 – 77 wt.% SiO_2
Phenocryst assemblage	Sodic sanidine + haüyne + clinopyroxene + biotite + titanite + magnetite	Sodic sanidine + quartz + clinopyroxene + magnetite + fayalite	Alkali feldspar + quartz + clinopyroxene ± fayalite
Melt silica saturation	*ne* = 27%	*Q* = 33%	*Q* = 30 - 35%
Melt (Na+K)/Al	0.99 ± 0.02	1.02 ± 0.03	1.00 – 1.03
Melt NBO/T**	0.26	0.25	0.24 – 0.25
Magma T, °C	825	700	800
Pressure, kbar	1	1.5	1
fO_2	NNO	QMF	~QMF
Pyroxene composition	Na-salite	Ferrohedenbergite	Ferroaugite - ferrohedenbergite
Pyroxene Mg#	48 – 58	14.2 – 16.2	9.6 – 31.7

References: [1]Edgar et al. (2007); [2]Warshaw & Smith (1988), Spell et al. (1996); [3]Streck & Grunder (1997).

*The BT pyroxenes and glasses in this study are taken from the first 120 km^3 of homogeneous magma ejected during the Otowi Member eruption. The total volume for the unit is ~450 km^3.

**NBO/T = (2O + 4T)/T, where O = total oxygen atoms and T = (Si + Al + Fe^{3+} + Ti) on a molar basis, and assuming 3% dissociated H_2O, corresponding to total magmatic water contents of 5% in each case (Sowerby & Keppler, 1999).

Table 2	FM phon. glass	FM Na-salite	FM Na-salite	RT rhyo. glass	RT ferroaug/hed	RT ferroaug/hed	BT rhyo. glass	BT ferrohed/aug	BT ferrohed/aug
Oxide	03TF16	99TF6gmB_PX2B	0154px1	RT173C	RT173B_1b	RT173C_4a	0086A	13/2_a	13/3_c
SiO_2	58.58	49.21	48.72	75.47	48.06	47.76	77.17	48.66	48.74
TiO_2	0.43	0.87	0.69	0.16	0.21	0.30	0.04	0.07	0.12
Al_2O_3	21.58	2.49	2.11	12.26	0.41	0.54	12.09	0.38	0.30
FeO	2.31	15.27	13.43	1.96	25.33	28.85	1.29	26.14	26.11
MnO	0.19	1.35	1.23	0.10	2.76	2.39	0.10	2.77	2.89
MgO	0.24	7.98	8.54	0.01	3.71	1.73	0.02	2.72	2.44
CaO	0.82	20.24	20.46	0.50	17.99	17.61	0.25	17.99	18.14
Na_2O	8.80	2.30	2.23	4.61	0.54	0.45	4.69	0.74	0.68
K_2O	5.84			4.69			4.35		
Totals	98.79	99.76	97.42	99.4	99.08	99.67		99.47	99.42
Cations									
Si		1.88	1.89		1.96	1.97		1.98	2.00
Al		0.11	0.10		0.02	0.03		0.02	0.01
Na		0.17	0.17		0.04	0.04		0.06	0.05
Ca		0.83	0.85		0.79	0.78		0.79	0.79
Mn		0.04	0.04		0.10	0.08		0.09	0.10
Fe^{2+}		0.24	0.19		0.77	0.93		0.84	0.87
Fe^{3+}		0.25	0.24		0.10	0.06		0.05	0.02
Mg		0.45	0.49		0.23	0.11		0.17	0.15
Ti		0.02	0.02		0.01	0.01		0.00	0.00
Cation total		4.00	4.00		4.00	4.00		4.00	4.00
Trace elements									
ppm Sc	b.d.l.	27	30	3.3	412	357	b.d.l.	155	60
Sr	33	3.8	3.7	18	3.9	11	0.1	0.08	0.05
Y	21	26	31	76	270	185	78	286	548
Zr	1393	1,363	2,062	350	64	77	204	35	86
Nb	239	2.8	3.0	25	0.09	0.09	185	0.31	0.90
Ba	88	0.43	0.36	1685	0.84	0.68	0.17	0.33	0.86
La	101	57	61	50	50	41	33	33	67
Ce	136	118	133	114	203	169	84	132	257
Pr	10	10.9	12.5	15	40	31	9.0	26	49
Nd	26	34	40	61	222	169	34	161	309
Sm	3.6	5.0	5.8	14	71	51	10	66	121
Eu	0.64	0.91	1.00	2.3	7.5	7.3	b.d.l.	0.16	0.21
Gd	n.d.	3.9	5.3	n.d.	67	46	n.d.	72	134
Tb	0.40	0.67	0.82	2.2	11	7.5	1.9	12	22
Dy	2.8	4.1	5.3	14	62	42	13	78	144
Ho	0.68	0.91	1.20	2.9	12	8.2	2.7	14	26
Er	2.3	3.0	4.2	8.1	31	22	8.0	36	67
Tm	0.38	0.66	0.95	1.2	4.7	3.4	1.2	5.3	10
Yb	3.3	8.0	11.0	8.0	35	26	8.5	41	81
Lu	0.53	1.9	2.8	1.3	7.9	6.1	1.2	7.9	16
Hf	23	34	47	9.4	2.4	2.9	10	2.7	10
Ta	7.0	0.19	0.34	1.5	b.d.l.	b.d.l.	11	b.d.l.	b.d.l.
Pb	22	0.54	0.41	13	0.72	0.59	35	1.3	2.2
Th	42	0.09	0.12	5.6	0.02	0.02	34	0.03	0.13
U	12	0.01	0.01	2.9	0.00	0.01	18	0.01	0.02

Table 3

Cation	VIII-fold ionic radius (Å)	VI-fold ionic radius (Å)
Na 1+	1.18	
Ca 2+	1.12	
Mn 2+		0.83
Fe 2+		0.78
Mg 2+		0.72
Ti 4+		0.605
La 3+	1.16	1.032
Ce 3+	1.143	1.010
Pr 3+	1.126	0.990
Nd 3+	1.109	0.983
Pm 3+	1.093	0.970
Sm 3+	1.079	0.958
Eu 3+	1.066	0.947
Gd 3+	1.053	0.938
Tb 3+	1.04	0.923
Dy 3+	1.027	0.912
Y 3+	1.019	0.900
Ho 3+	1.015	0.901
Er 3+	1.004	0.890
Tm 3+	0.994	0.880
Yb 3+	0.985	0.868
Lu 3+	0.977	0.861
Sc 3+		0.745
Zr 4+		0.72
Hf 4+		0.71
Nb 5+		0.64
Ta 5+		0.64

Table 4

Model Values	FM Na-salites	RT ferroaugites	BT ferrohedenbergites
T °C	825	800	700
$^{VIII}E^{3+}_{M2}$ GPa	177	296	339
$^{VIII}r_0$ Å	1.060	1.055	1.055
$^{VIII}D_0$	1.6	5.2	9.0
$^{VI}E^{3+}_{M}$ GPa	775	1000	1100
$^{VI}r_0$ Å	0.724	0.758	0.772
$^{VI}D_0$	500	150	200

Table 5 **Pyroxene – Glass Partition Coefficients**

	FM Na-salites (n=31)				RT ferroaug/hed (n=40)				BT ferrohed/aug (n=67)			
Element	**Max**	**Min**	**Ave**	**Model**	**Max**	**Min**	**Ave**	**Model**	**Max**	**Min**	**Ave**	**Model**
Sc	n.d.	n.d.	n.d.	n.d.	186	93	143	139	n.d.	n.d.	n.d.	n.d.
Ti	1.9	0.8	1.3	n.d.	2.0	1.2	1.5	n.d.	2.0	1.3	1.6	n.d.
Y	1.5	0.9	1.3	1.5	4.8	2.1	3.6	4.5	7.2	3.8	4.8	7.4
Zr	1.7	0.7	1.2	n.d.	0.3	0.2	0.2	n.d.	0.4	0.2	0.3	n.d.
Nb	0.04	0.01	0.02	n.d.	0.005	0.002	0.003	n.d.	0.019	0.001	0.004	n.d.
La	0.7	0.4	0.6	0.6	1.2	0.7	1.0	1.1	2.3	0.9	1.2	1.3
Ce	1.1	0.5	0.8	0.8	2.0	1.2	1.7	1.8	3.9	1.5	1.9	2.3
Pr	1.5	0.7	1.1	1.0	3.3	1.7	2.6	2.6	6.9	2.9	3.6	3.7
Nd	2.2	0.9	1.3	1.3	4.9	2.3	3.7	3.5	11	4.4	5.6	5.4
Sm	2.4	1.0	1.5	1.5	6.6	2.9	5.0	4.8	16	6.3	8.0	8.2
Eu	2.6	1.0	1.4	1.6	7.6	5.6	6.5	5.1	128	n.d.	n.d.	8.8
Gd	n.d.	n.d.	n.d.	1.6	n.d.	n.d.	n.d.	5.2	n.d.	n.d.	n.d.	9.0
Tb	2.2	1.2	1.6	1.6	6.6	2.8	5.0	5.1	13	6.6	7.9	8.7
Dy	2.1	1.1	1.5	1.5	6.2	2.6	4.6	4.7	12	6.1	7.6	7.9
Ho	2.2	1.1	1.5	1.5	5.7	2.4	4.2	4.3	10	5.5	6.6	7.0
Er	2.1	1.2	1.6	1.5	5.2	2.3	3.9	4.0	9.2	4.9	6.2	6.4
Tm	2.8	1.5	2.1	1.9	5.1	2.3	3.8	4.0	9.2	4.8	6.3	6.2
Yb	3.6	2.4	2.9	3.1	5.7	2.8	4.4	4.9	11	5.4	7.4	7.9
Lu	5.9	3.5	4.5	4.6	7.9	4.0	6.1	6.1	14	7.2	10	9.8
Hf	2.6	1.0	1.8	n.d.	0.4	0.2	0.3	n.d.	1.0	0.3	0.4	n.d.
Ta	0.16	0.01	0.05	n.d.	n.d.	n.d.	n.d.	n.d.	n.d.	n.d.	n.d.	n.d.

Table 6

Cation(coord#)	**α, Å^3**	**$\Delta = [\alpha_{(\text{light ion})} - \alpha_{(\text{heavy ion})}]/\alpha_{(\text{light ion})}$**	
Y^{3+}(VI)	2.12	Δ Y-Dy(VI)	-0.0896
Y^{3+}(VIII)	1.844	Δ Y-Dy(VIII)	-0.1236
Zr^{4+}	2.023	Δ Y-Ho(VI)	-0.0566
Nb^{5+}	3.10	Δ Y-Ho(VIII)	-0.0906
Dy^{3+}(VI)	2.31	Δ Y-Er(VI)	-0.0283
Dy^{3+}(VIII)	2.072	Δ Y-Er(VIII)	-0.0553
Ho^{3+}(VI)	2.24	Δ Zr-Hf	0.0657
Ho^{3+}(VIII)	2.011	Δ Nb-Ta	0.0903
Er^{3+}(VI)	2.18		
Er^{3+}(VIII)	1.946		
Hf^{4+}	1.89		
Ta^{5+}	2.82		